Flash-within-flash synthesis of gram-scale solid-state materials

Chi Hun Choi[1], Jaeho Shin[2], Lucas Eddy[3], Victoria Granja[4], Kevin Wyss[2], Bárbara Damasceno[2], Hua Guo[1], Guanhui Gao[1], Yufeng Zhao[5], C. Fred Higgs III[4], Yimo Han[1]*, and James M. Tour[1,2,6]*

Affiliations:

[1]*Department of Materials Science and Nanoengineering, Rice University, 6100 Main Street, Houston, Texas 77005, USA*
[2]*Department of Chemistry, Rice University, 6100 Main Street, Houston, Texas 77005, USA*
[3]*Applied Physics Graduate Program, Smalley-Curl Institute, Rice University, Houston, Texas 77005, USA*
[4]*Department of Mechanical Engineering, Rice University, 6100 Main Street, Houston, TX 77005, USA*
[5]*Corban University, 5000 Deer Park Drive SE, Salem, OR 97317 USA*
[6]*Smalley-Curl Institute, NanoCarbon Center and The Rice Advanced Materials Institute, Rice University, 6100 Main Street, Houston, Texas 77005, USA*

*Email: tour@rice.edu, yh76@rice.edu

Abstract:

Sustainable manufacturing that prioritizes energy efficiency, minimal water use, scalability, and the ability to generate diverse materials is essential to advance inorganic materials production while maintaining environmental consciousness. However, current manufacturing practices are unable to meet these requirements. Here, we describe a new flash-within-flash Joule heating (FWF)—a non-equilibrium, ultrafast heat conduction method—to prepare 13 transition metal dichalcogenides (TMD) and 9 non-TMD materials, each in under 5 seconds while in ambient conditions. FWF achieves enormous advantages in facile gram scalability and in sustainable manufacturing criteria when compared to other synthesis methods. Also, FWF allows the production of phase-selective and single-crystalline bulk powders, a phenomenon rarely observed by any other synthesis method. Furthermore, FWF-made $MoSe_2$ outperformed commercially available $MoSe_2$ in tribology, showcasing the quality of FWF-made materials. The capability for atom substitution and doping further highlights the versatility of FWF as a general bulk inorganic materials synthesis protocol.

1

Introduction

The next generation of synthesis protocols must meet three main criteria to afford minimal environmental impact: reduced use of solvents and water, improved energy efficiency, and scalability[1,2]. These requirements are often hard to achieve using equilibrium states of thermodynamics since many synthetic processes require high temperatures (>600 °C) or extended reaction times ranging from hours to days. Recent non-equilibrium syntheses that use rapid thermal shock via ultrafast resistive Joule heating have surfaced as more promising methods to produce specific products, including ceramics[3,4], metastable materials[5,6], and value-added chemicals and materials[7–9]. These established methods are conducted in milliseconds to minutes, thereby showing substantial reductions in energy use. However, these protocols often need to meet specific electrical conductivity requirements, thereby limiting the reagents that can be used. To bypass this limitation, the introduction of conductive additives or substrate is necessary, which results in impurities and difficulty in obtaining standalone products. Furthermore, the incorporation of volatile reagents such as chalcogens (e.g., S and Se) is difficult to realize due to the intensive heat caused by resistive heating, constraining these elemental incorporations.

Results and Discussion

Here, we introduce a general, non-equilibrium flash-within-flash Joule heating (FWF) synthesis protocol as an ultrafast heat conduction mechanism that allows a rapid synthesis of various compounds in seconds (**Fig. 1a**). The process involves using two quartz vessels: an outer flashing vessel filled with an inexpensive conductive feedstock, such as metallurgical coke, and an inner, semi-closed reactor that contains the target reagents. During the FWF process, the system is in an ambient atmosphere and flash Joule heating (FJH) is applied to the outer vessel. The current passes through the conductive feedstock in the outer vessel, leading to resistive Joule heating and

the generation of high temperatures of ~2000 °C as measured by an infrared camera (**Fig. 1b**). The intense heat produced in the outer vessel's metallurgical coke then transfers to the inner vessel through thermal conduction, allowing for ultrafast heating of the reagents in the inner tube (**Fig. S1**). The pulsated discharge through duty cycles (**Fig. S2a-c**) allows continuous change in temperature, pressure, and volume with respect to the input voltage to trigger the non-equilibrium, kinetically controlled reaction while forming specific targeted products in the inner vessel. Concurrently, the outer metallurgical coke turns into turbostratic graphene (**Fig. S3a-b**) to give additional value-added chemicals in a single reaction. The entire process takes place in just under 5 s, highlighting the ultrafast kinetics of FWF.

FWF can be further fine-tuned. By adapting three different reaction designs, certain issues such as slow rates and side reactions can be mitigated, thereby producing materials that have been difficult to prepare by other methods. Type 1 was described above. Type 2 reaction (**Fig. 1c**) includes flashing 2 to 5 times in succession, addressing the issue of partial conversion. For example, the initial attempt for converting tungstic acid ($WO_3 \cdot H_2O$) to WS_2 did not result in full conversion, as shown by the presence of unreacted precursors in the XRD analysis (**Fig. S4**). This could be attributed to the slow reaction rate. However, upon performing sequential FWF reactions, a near full conversion was achieved. The XRD data illustrates that the signal of the starting WO_3 (denoted in **Fig. S4** inset) decreases with each subsequent reaction, suggesting nearly complete conversion of WO_3 to WS_2 over three FWF reaction cycles. Type 3, an anion-exchange reaction, can also address reactions that pose difficulties due to unexpected side reactions (**Fig 1d**). For example, the side reaction from $Bi(NO_3)_3 \cdot 5H_2O$ and Se leads to an evolution of a brown gas (all reactions were conducted in a well-ventilated fume hood). After performing FWF with these solid precursors, the resultant product was a mixture of $BiSeO_2$ and $BiSeO_5$ (**Fig. S5**), suggesting that the gas evolution

3

was due to an unexpected oxidative reaction. This unwanted oxidation reaction was successfully bypassed by using the reaction Type 3. Bi_2Se_3 was synthesized using $Bi(NO_3)_3 \cdot 5H_2O$ and SeS_2, which initially yielded $Bi_2S_xSe_y$. This intermediate was then treated with Se to facilitate anion-exchange reactions. Similarly, by changing the added chalcogen to S, Bi_2S_3 was afforded. The X-ray diffraction (XRD) analysis indicates that the full conversion occurred to produce either pure Bi_2S_3 or pure Bi_2Se_3, as desired (**Fig. S6**).

An exceptional advantage of the FWF method is its scalability to gram-scale production without complications. Such high scalability is rarely observed in laboratory chemical syntheses, which often require additional engineering, apparatus setup, and/or alternative synthesis routes to ensure complete conversion of the materials[10,11]. In contrast, FWF can be easily scaled by adjusting the voltage to accommodate the increase in reactant mass. Also, the semi-closed inner reactor allows efficient outgassing, playing a critical role in allowing the incorporation of highly volatile reagents like chalcogens. Furthermore, outgassing prohibits oxygen infiltration and prevents cracking of the inner tube. We demonstrate the scalability of FWF by synthesizing WSe_2 from W and Se precursors and successfully achieved facile gram-scale production (See **Supplementary Methods**, **Fig. 2a-d**). **Fig. 2a** shows 1.11 g of WSe_2 that was synthesized in a single reaction. XRD analysis (**Fig. 2b**) and X-ray photoelectron spectroscopy (XPS) spectra (**Fig. 2c-d**) show highly pure, crystalline WSe_2 with no discernible byproduct or remnant of initial precursors. This demonstration highlights the remarkable scalability of the FWF method.

A comprehensive life cycle assessment (LCA) was conducted (See **Supplementary Discussion**, **Fig. S7-9,** and **Table S1-6**) to compare the sustainability of FWF with the Mg-assisted autoclave synthesis[12] and chemical vapor transport (CVT) method[13] for synthesizing 100 g of $MoSe_2$[14]. These two methods were chosen because the final product exhibits similar characteristics

4

such as multilayers and high crystallinity. The cradle-to-gate LCA categorized the cumulative energy demand (**Fig. 2e**), global warming potential (**Fig. 2f**), and cumulative water usage (**Fig. 2g**). The LCA demonstrates that the FWF synthesis of $MoSe_2$ uses 56-83% less energy, produces 71-94% less greenhouse gases, and consumes 90-97% less water, compared to autoclave and CVT methods, respectively. A preliminary production cost (**Fig. 2h**) was afforded by a techno-economic assessment (TEA). The preliminary TEA reveals that FWF offers large cost savings for the preparation of inorganic materials, making FWF an attractive consideration for manufacturing.

The FWF method can be used for the general synthesis of various compounds. So far, by controlling the voltages and reagents alone, 13 TMDs and 9 non-TMD materials have been prepared (**Fig. 3a, Table S7**). XRD, XPS and/or (scanning) transmission electron microscopy (S/TEM) characterizations indicate successful synthesis (**Fig S10-32**), highlighting the consistent production of desired products. Diverse solid-state reagents can be employed including metal powders (e.g., Ni, Mo, W), metal chlorides (e.g., $SnCl_2 \cdot 2H_2O$), metal oxides (e.g., cobalt (II, III) oxide, iron oxide hydrate), metal nitrates (e.g., $Bi(NO_3)_3 \cdot 5H_2O$), and hydrated salts as the precursors. The voltage for each reaction was optimized to produce the desired final product (**Fig. 3b**). This versatile synthesis technique overcomes not only the conductivity requirements and carbothermic reduction of many thermal shock methods including FJH, but also limitations of other synthesis protocols such as hydrothermal synthesis where solubility and type of initial precursors play critical roles in forming the product of interest[15]. Even though most of the compounds synthesized in this experiment focused on the TMDs and layered materials[16,17], the formation of non-TMD materials, including titanium nitride (TiN) and lanthanum borate ($LaBO_3$), was demonstrated suggesting that FWF could serve as a general method for synthesizing a wide variety of inorganic compounds.

Doping (substitution) of various compounds using FWF is also possible by simply changing the initial precursor. Three different chalcogens, S, SeS_2, and Se, were used as the corresponding anions in the Sn-based system to observe reagent-dependent tunability and doping capabilities (see **Supplementary Methods**, **Fig. 3c-e**). As shown in annular dark field scanning transmission electron microscopy (ADF-STEM) and energy dispersive X-ray spectrometry (EDX), the atomic resolution images of SnS_2 (**Fig. 3c**) and $SnSe_2$ (**Fig. 3d**) indicate that the syntheses of these compounds were successful; EDX also suggests similar results with the ADF-STEM imaging detecting Sn and S or Se, respectively. Remarkably, by simply substituting the initial precursor to SeS_2, Se-doped SnS_2 (denoted as SnS_xSe_y) was formed (**Fig. 3e**). The EDX spectrum indicates the uniform distribution of Se with high crystallinity as observed in the ADF-STEM image. Due to the 2:1 ratio between S and Se, the Raman spectrum and XRD of SnS_xSe_y exhibits similar features as the SnS_2 (**Fig. S13**). However, as shown in the inset of **Fig. S13**, the color of the powders dramatically changed from yellow (SnS_2) to red (SnS_xSe_y), indicating that doping and misalignment of the two-dimensional sheets result in the bandgap shift in the material[18,19]. This provides a simple and fast method to dope other atoms into the system, suggesting a doping procedure for applications in electronics[20], catalysis[21], and energy storage[22,23].

FWF allows phase controlled TMD synthesis. ADF-STEM of $MoSe_2$ and WSe_2 (**Fig. 3f-g**) indicate that these materials exhibit hexagonal atomic configuration along with 2H-phase and AB stacking, presenting their energy favorable structure in the analyzed flake[24]. In contrast to the previous FJH method that produced metastable graphene with turbostratic configuration[7], the FWF does not involve electric current passing through the sample during synthesis. This might account for the highly regular order in stacking. For In_2Se_3, as suggested by XRD (**Fig. S26**) and ADF-STEM images (**Fig. 3h**), only alpha phase (α-In_2Se_3) is present in the flakes, suggesting that the

presently optimized FWF is a selective process. Additionally, all analyzed flakes exhibited single-crystalline orientation (**Fig. S33**), further showcasing the ability of FWF to produce phase-selective and single-crystalline bulk powders, a result rarely observed in other non-equilibrium methods.

Understanding the electrical properties of FWF products is critical since these synthesized materials can be widely adopted in numerous applications. $MoSe_2$, WSe_2, and α-In_2Se_3 flakes were targeted because they exhibit n-type semiconductor, p-type semiconductor, and ferroelectricity behaviors, respectively. To characterize the electrical properties, FWF materials were exfoliated by mechanical exfoliation, and field-effect transistor (FET) devices were fabricated by conventional photolithographic methods on a SiO_2/Si substrate (**Fig. 4**). The details of the device fabrication procedure are discussed in the **Methods** section. Cross-sectional ADF-STEM and energy dispersive X-ray spectrometry (EDX) analysis were performed to obtain atomic resolution images of the devices along with their constituents (**Fig. 4b, Fig. S34**), showing the layered structure, clean interfaces, and homogeneous atomic distribution. To verify the electrical characteristics of as-synthesized materials, the transfer and output curves are investigated. For $MoSe_2$, the transfer curve displayed an ON-current when a positive gate bias was applied regardless of drain voltages (**Fig. 4c**). In addition, the output curve showed higher drain current when the gate bias was positive (**Fig. 4f**), indicative of its n-type characteristics[25]. Conversely, for WSe_2, the transfer curve exhibited an ON-current when a negative gate bias was applied regardless of drain voltages (**Fig. 4d**). Similarly, the output curve showed higher current when the gate bias was negative (**Fig. 4g**), indicating typical p-type characteristics[26]. This suggests that the FWF technique can generate n-type and p-type semiconducting flakes, achieving an ON/OFF ratio of

1.1×10^6 and mobility of 6.81 $cm^2 \cdot V^{-1} \cdot s^{-1}$ for MoSe$_2$. For WSe$_2$, an ON/OFF ratio of 1.74×10^4 and mobility of 2.96 $cm^2 V^{-1} s^{-1}$ were achieved. (**Fig. S35**).

In the case of α-In$_2$Se$_3$ (**Fig. 4e**), the transfer curve demonstrated an ON-current with a positive gate bias, which is typical n-type semiconducting behavior. However, the curve also exhibited a clockwise hysteresis loop due to the ferroelectric characteristics of α-In$_2$Se$_3$[27]. We further conducted the endurance test to observe the SET/RESET characteristic of α-In$_2$Se$_3$. As shown in **Fig. 4h** (See **Methods**), no degradation of performance was observed for 1,000 cycles with an ON/OFF ratio of ~10^2, suggesting a high durability that is comparable to chemical-vapor-deposition-grown α-In$_2$Se$_3$[27]. The results suggest that the non-equilibrium FWF produced materials exhibit outstanding electrical properties that could facilitate the development of various devices with metal chalcogenides and promote fundamental research of these materials, now easily accessible in gram-scale with lowered cost.

A comparative analysis of coefficient of friction (COF) was made between the commercially available MoSe$_2$ and FWF MoSe$_2$ to demonstrate superior and stable tribological performance. As shown in **Fig. 5a**, in the initial stages of the test, the COF for commercial MoSe$_2$ and FWF MoSe$_2$ were effectively indistinguishable. However, after 2 min into operation, a noticeable increase in COF for commercially available MoSe$_2$ was observed. Similarly, FWF MoSe$_2$ outperformed commercially available MoSe$_2$ under different loads (**Fig. 5b**). The coefficient of friction exhibited a reduction of 69%, 20%, and 41% at applied loads of 1 N, 5 N, and 10 N, respectively. This result suggests that the commercially available MoSe$_2$ film degraded and/or abraded at a faster rate than the FWF MoSe$_2$ film, suggesting that the quality of the initial powders differed. This superior and stable performance might be due to the single-crystalline nature of FWF MoSe$_2$, resulting in an overall lower coefficient of friction and enhanced

8

tribological performance[28–30]. Due to the well-defined lamellar orientation of the FWF $MoSe_2$ coating material, these sheets can easily slide atop one another, thereby reducing resistance to motion, and consequently the coefficient of friction.

Conclusion

In conclusion, FWF overcomes the limitations of traditional equilibrium-based large-scale synthesis methods, enabling faster reaction rates and reduced reliance on solvents, water, and energy. FWF also offers a versatile, efficient, and scalable protocol for producing a wide range of inorganic compounds with exceptional control over synthesis parameters to produce phase-selective and single-crystalline bulk powders. FWF demonstrates flexibility in materials modification through doping and gram scalability, holding promise for environmentally friendly access to designed inorganic materials with enormous cost savings. Finally, diverse applications can be realized with FWF-made materials as showcased as an example of FWF $MoSe_2$ outperforming commercially available $MoSe_2$ in tribological performance.

Online content

Any methods, additional references, Nature Portfolio reporting summaries, source data, extended data, supplementary information, acknowledgements, peer review information; details of author contributions and competing interests; and statements of data and code availability are available at https://doi.org/10.xxxx/xxxxxx-xxx-xxxxx-x.

Reference

1. Raabe, D. The materials science behind sustainable metals and alloys. *Chem. Rev.* **123**, 2436–2608 (2023).

2. Aykol, M., Montoya, J. H. & Hummelshøj, J. Rational solid-state synthesis routes for inorganic materials. *J. Am. Chem. Soc.* **143**, 9244–9259 (2021).

3. Wang, C. *et al.* A general method to synthesize and sinter bulk ceramics in seconds. *Science* **368**, 521–526 (2020).

4. Deng, B. *et al.* High-surface-area corundum nanoparticles by resistive hotspot-induced phase transformation. *Nat. Commun.* **13**, 5027 (2022).

5. Zheng, X. *et al.* Hydrogen-substituted graphdiyne-assisted ultrafast sparking synthesis of metastable nanomaterials. *Nat. Nanotechnol.* **18**, 153–159 (2023).

6. Chen, W. *et al.* Millisecond conversion of metastable 2D materials by flash Joule heating. *ACS Nano* **15**, 1282–1290 (2021).

7. Luong, D. X. *et al.* Gram-scale bottom-up flash graphene synthesis. *Nature* **577**, 647–651 (2020).

8. Deng, B. *et al.* Phase controlled synthesis of transition metal carbide nanocrystals by ultrafast flash Joule heating. *Nat. Commun.* **13**, 262 (2022).

9. Wyss, K. M. *et al.* Synthesis of clean hydrogen gas from waste plastic at zero net cost. *Adv. Mater.* e2306763 (2023) doi:10.1002/adma.202306763.

10. Li, L. *et al.* Kilogram-scale synthesis and functionalization of carbon dots for superior electrochemical potassium storage. *ACS Nano* **15**, 6872–6885 (2021).

11. Eddy, L. *et al.* Laboratory kilogram-scale graphene production from coal. (2023) doi:10.26434/chemrxiv-2023-7z1s2.

12. Upadhyay, S. & Pandey, O. P. Synthesis of layered 2H–MoSe$_2$ nanosheets for the high-performance supercapacitor electrode material. *J. Alloy. Compd.* **857**, 157522 (2021).

13. Ubaldini, A. & Giannini, E. Improved chemical vapor transport growth of transition metal dichalcogenides. *J. Cryst. Growth* **401**, 878–882 (2014).

14. Hellweg, S. & Canals, L. M. i. Emerging approaches, challenges and opportunities in life cycle assessment. *Science* **344**, 1109–1113 (2014).

15. Joo, J., Chow, B. Y., Prakash, M., Boyden, E. S. & Jacobson, J. M. Face-selective electrostatic control of hydrothermal zinc oxide nanowire synthesis. *Nat. Mater.* **10**, 596–601 (2011).

16. Du, Z. *et al.* Conversion of non-van der Waals solids to 2D transition-metal chalcogenides. *Nature* **577**, 492–496 (2020).

17. Feng, Y. *et al.* Synthesis of noble metal chalcogenides via cation exchange reactions. *Nat. Synth.* **1**, 626–634 (2022).

18. Chen, X., Liu, L., Yu, P. Y. & Mao, S. S. Increasing solar absorption for photocatalysis with black hydrogenated titanium dioxide nanocrystals. *Science* **331**, 746–750 (2011).

19. Choi, C. H. *et al.* Polymeric carbon nitride with localized aluminum coordination sites as a durable and efficient photocatalyst for visible light utilization. *ACS Catal.* **8**, 4241–4256 (2018).

20. Shi, W. *et al.* Reversible writing of high-mobility and high-carrier-density doping patterns in two-dimensional van der Waals heterostructures. *Nat. Electron.* **3**, 99–105 (2020).

21. Dou, Y. *et al.* Approaching the activity limit of $CoSe_2$ for oxygen evolution via Fe doping and Co vacancy. *Nat. Commun.* **11**, 1664 (2020).

22. Zhu, L.-F. *et al.* Heterovalent-doping-enabled atom-displacement fluctuation leads to ultrahigh energy-storage density in $AgNbO_3$-based multilayer capacitors. *Nat. Commun.* **14**, 1166 (2023).

23. Zhu, W. *et al.* Ultrafast non-equilibrium synthesis of cathode materials for Li-ion batteries. *Adv. Mater.* **35**, 2208974 (2023).

24. Förg, M. *et al.* Moiré excitons in $MoSe_2$-WSe_2 heterobilayers and heterotrilayers. *Nat. Commun.* **12**, 1656 (2021).

25. Jung, C. *et al.* Highly crystalline CVD-grown Multilayer $MoSe_2$ thin film transistor for fast photodetector. *Sci. Rep.* **5**, 15313 (2015).

26. Kim, K. S. *et al.* Non-epitaxial single-crystal 2D material growth by geometric confinement. *Nature* **614**, 88–94 (2023).

27. Si, M. *et al.* A ferroelectric semiconductor field-effect transistor. *Nat. Electron.* **2**, 580–586 (2019).

28. Liu, Y. *et al.* Interlayer friction and superlubricity in single-crystalline contact enabled by two-dimensional flake-wrapped atomic force microscope tips. *ACS Nano* **12**, 7638–7646 (2018).

29. Lee, C. *et al.* Frictional characteristics of atomically thin sheets. *Science* **328**, 76–80 (2010).

30. Huang, Y. *et al.* Single-crystalline 2D erucamide with low friction and enhanced thermal conductivity. *Colloids Surf. A: Physicochem. Eng. Asp.* **540**, 29–35 (2018).

Methods

Flash Joule Heating Equipment & Calculation of Energy Delivered

The flash Joule heating reactions were performed by a custom-built system using capacitor banks to deliver the flash. 48 Kemet ALS70A133QT500 capacitors, each rated at 13 mF and 500 V, were connected in parallel (624 mF total) and charged to the desired voltage. A variable frequency driver controlled the discharge intensity using pulse width modulation by using a duty cycle pattern operating at 1 kHz of 10 % intensity for 1 s, followed by 20% for 0.5 s, and finally 50 % for 5 s. It should be noted that almost all the voltage is used during the 10% and 20% duty cycle; the 50% duty cycle is to ensure all the voltage is discharged through the sample. The duty cycles, charging, and flashing operations were controlled by a custom LabVIEW program. The current discharged during flashing was measured using a Tamura L34S1T2D15 Hall effect sensor. The temperature was measured using a Micro-Epsilon CTRM1H1SF100-C3 pyrometer. The total amount of energy delivered to the reaction can be calculated by using the below equation:

$$\frac{\frac{1}{2}CV^2}{Total\ Mass\ of\ Metcoke}$$

where C is the capacitance (624 mF) and V is the flashing voltage. For example, when flashing at 340 V, the total amount of energy delivered is ~7.2 kJ/g. Since the current does not flow through the inner tube, the inner tube mass contribution is negligible.

Characterization

To analyze the crystallinity and the composition of the resultant powders after the FWF reactions, powder X-ray diffraction (pXRD) spectra were collected using Rigaku SmartLab XRD with CuKα radiation. All the XRD spectra were collected from 2θ angle of 3° to 80°. X-ray photoelectron spectra (XPS) were acquired using PHI Quantera SXM Scanning X-ray Microprobe with a base pressure of 5×10^{-9} Torr. All XPS spectra were corrected using carbon 1s (284.8 eV) peak as a reference. Annular dark field scanning transmission electron microscope (ADF-STEM) images were collected by FEI Titan Themis S/TEM system operating at 300 keV. The powder samples were prepared by drop-casting 300 μL of aliquot (1 mg of sample/1 mL ethanol) on Cu/lacey carbon TEM grid (Ted Pella). The resultant grid was dried at 80 °C on a hotplate for an hour with subsequent overnight vacuum drying. For cross-sectional samples, focused ion beam (FIB) cutting was performed with FEI Helios NanoLab 660 DualBeam system. The resultant FIB cross-section sample was attached to the PELCO® Cu half grids (Ted Pella) for further characterization under ADF-STEM. Finally, Raman spectra were collected using a Renishaw Raman microscope (532-nm laser, 50x lens) with the as-synthesized samples on top of a slide glass.

Device Fabrication

The $MoSe_2$, WSe_2, and In_2Se_3 samples were prepared using the typical mechanical exfoliation method on SiO_2 (285 nm)/Si substrate, respectively. The thickness of their layers was verified by optical contrast, following which the cross-sectional TEM was used to determine the thickness of them. To make the electrical contact, a conventional photolithography was used to make the source

and drain patterns where the channel length is 3 μm, and 50 nm of Au metal was deposited by an electron beam evaporator under a pressure of ~10^{-8} Torr and deposition rate of 2.0 Å/s. To remove the residual photoresist, the sample was immersed in acetone bath for 6 h ~ 12 h, and then the solution was gently blown by N_2 gas. Finally, to enhance the interfacial contact properties between metal/2D materials, the fabricated devices were stored for 6 h ~ 12 h under vacuum (~ 10^{-3} Torr) conditions.

Electrical Measurements

The electrical characteristics were measured with a semiconductor parameter analyzer (Agilent B1500A Semiconductor Device Analyzer) and a probe station system under darkness to avoid the generation of photo-excited electrons and holes in 2D materials. The source electrode was grounded, drain voltage was applied by drain electrode, and the Si substrate was used to backgate electrode. To measure the endurance characteristics of In_2Se_3 FET, the gate voltage of -40 V with pulse width of 1 s was applied to make the SET state, and the channel current was subsequently measured by drain voltage of 1 V. After that, the gate voltage of +40 V with pulse width of 1 s was applied to make the RESET state, and the channel current was subsequently measured by drain voltage of 1 V. We repeated this sequence 1,000 times and investigated the endurance characteristics of In_2Se_3 FET devices.

Life Cycle Assessment (LCA)

A prospective LCA was conducted for $MoSe_2$ produced from FWF and compared to $MoSe_2$ produced by chemical vapor transport and autoclave synthetic methods. The study goal was to compare the cradle-to-gate impacts among these three different synthetic methods, and therefore use and disposal of the $MoSe_2$ was excluded. A functional unit of 100 g of powder was used since the industrial demand and implementation of the material is relatively small, including annual international production amounts. The cumulative energy demand, global warming potential over a 100-year timescale, and cumulative water use are evaluated. Process input and output data for each method were based on published literature methods[12–14]. Material transport and waste stream disposal or remediation are outside the scope of this limited study. Similarly, the scope and life cycle inventory of this LCA does not include one-time impacts such as factory construction and land use, or manufacturing of the one-time components and machines necessary to produce the raw materials or carryout the process workflow. This scope also does not include plant burdens, such as HVAC, lighting, supporting activities for materials handling, quality control, or packaging. Background data was primarily sourced from the Argonne National Lab GREET model including the software and spreadsheet models. A detailed spreadsheet, as well as further discussion of the scope and methodology of the LCA and TEA can be found in **Supplementary Text**, **Fig. S7-9**, and **Table S1-6**.

Tribology Performance Measurement

The samples are prepared by coating alumina substrates with commercial $MoSe_2$ powder and FWF $MoSe_2$ powder. The powder is directly applied onto the substrates and meticulously spread by

13

rubbing it against the surface for 5 minutes in a circular motion to disrupt heterogeneity and achieve the incorporation of the additive as a coating. To evaluate the tribological properties of the samples in sliding reciprocating motion, we use a tribometer with a ball-on-flat configuration. In this test, a 6 mm diameter chrome steel 52100 ball is slid against a rectangular flat alumina sample under different load conditions: 1 N, 5 N, and 10 N, at a frequency of 3 Hz for 10 minutes. The coefficient of friction is measured and reported as a function of time, with a sampling rate of 100 data points per second. The mass of the coating is 0.2 g.

Use of Large Language Model (ChatGPT)

The authors used ChatGPT to rephrase and correct spelling/grammar errors to ensure a clearer depiction of the work. The authors ensured that the final manuscript was in agreement with the technical and scientific knowledge.

Author contributions
C.H.C. first came up with the idea with L.E., realized the first demonstration of flash-within-flash Joule heating, conducted the synthesis of 22 materials, gram scalability, Raman, XRD, STEM, SAED, and EDX characterization, and manuscript writing under the guidance of J.M.T. and Y.H.; J.S. performed the device fabrications and electrical measurements for $MoSe_2$, WSe_2, and In_2Se_3 materials and aided the synthesis of In_2Se_3; L.E. managed the FJH system and aided C.H.C. with the synthesis; V.G. performed the tribological experiments to analyze the coefficient of friction. K.W performed LCA analysis; B.D. acquired and analyzed the XPS data; H.G. performed FIB for cross-section STEM sample preparation. G.G. aided C.H.C. in initial STEM characterization. Y.Z. contributed to the discussion of ultrafast thermal conduction pathway. C.F.G.III supervised V.G. in performing and analyzing tribological data. Y.H. supervised C.H.C. in microscopy analysis and guided C.H.C. in manuscript writing and figures. J.M.T. supervised C.H.C. in material synthesis, guided C.H.C. in manuscript writing, and oversaw the entire project.

Competing interests

Rice University has filed patents on the FWF process, but that process is presently unlicensed. Thus, authors declare no competing interests.

Additional information

Supplementary Information The online version contains supplementary material available at https://doi.org/10.xxxx/xxxxxx-xxx-xxxxx-x.

Peer Review Information

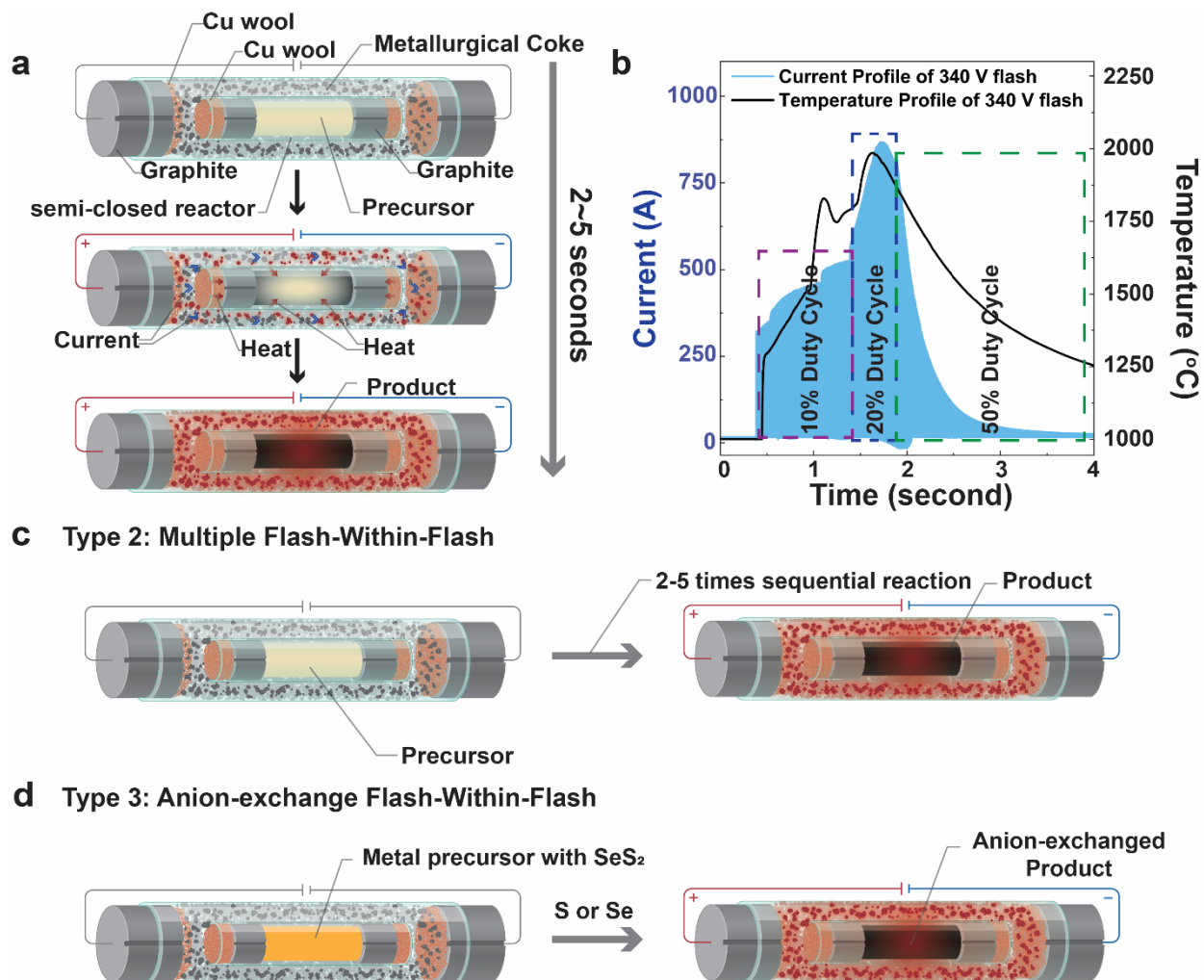**Reprints and permissions information** is available at http://www.nature.com/reprints

Fig. 1. Flash-within-flash Joule heating (FWF). a. A schematic description of FWF. **b.** The current (denoted in blue) and temperature profile (denoted in black) of 340 V FWF reaction. The dashed boxes indicate the regions of different duty cycles (e.g., purple box corresponds to 10% duty cycle region). **c.** A schematic description of Type 2: Multiple FWF reaction for allowing full conversion of unreacted precursors. **d.** A schematic description of Type 3: Anion-exchange FWF reaction for bypassing unexpected side reactions.
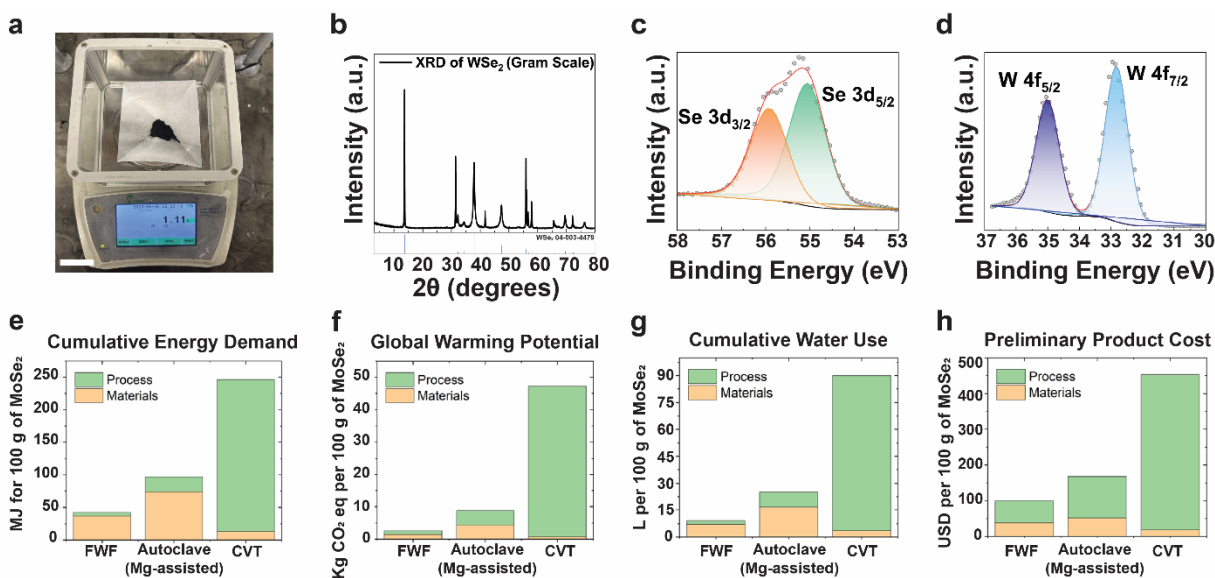
Fig. 2. Gram scalability and life cycle assessment. a. A photograph of 1.11 g of WSe$_2$ powder in an analytical balance obtained from the gram-scale reaction. The scale bar is 10 cm. **b.** XRD spectrum of WSe$_2$ made through a gram-scale reaction. A reference spectrum is provided below. **c.** Se 3d XPS spectrum of WSe$_2$ powder made through a gram-scale reaction. **d.** W 4f XPS spectrum of WSe$_2$ powder made through a gram-scale reaction. **e.** Cumulative energy demand analysis, **f.** global warming potential analysis, **g.** cumulative water use analysis, and **h.** preliminary estimated product cost (techno-economic analysis) of FWF compared with autoclave (Mg-assisted) and chemical vapor transport (CVT) syntheses for producing 100 g of MoSe$_2$.
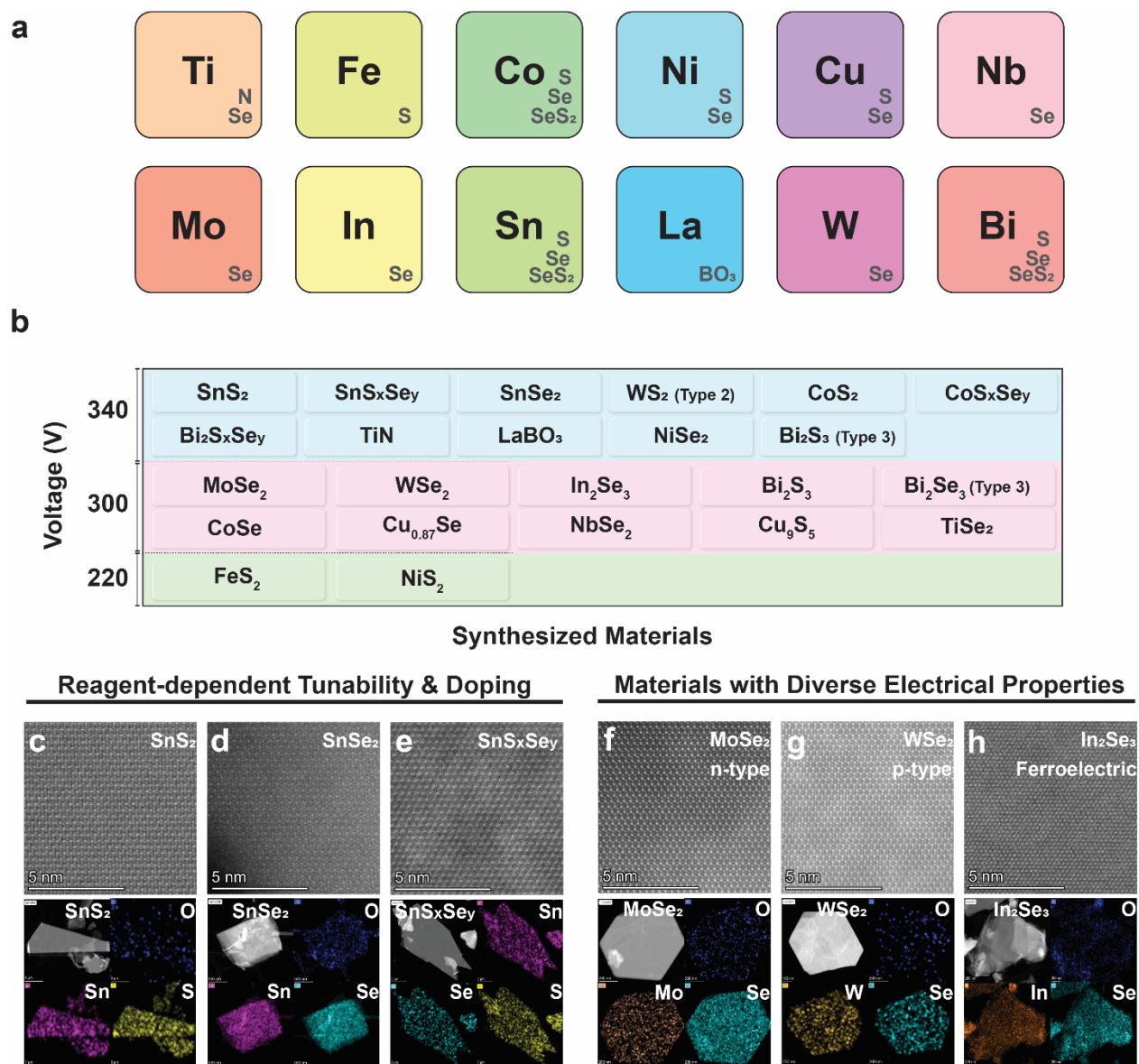
Fig. 3. Diverse reactions and products from FWF. a. A list of elements used here for the FWF reactions. The small subsets indicate the corresponding anion constituents used to make the inorganic compounds. **b.** The list of all the final products with respect to the initial flashing voltage. All the syntheses used Type 1 FWF unless otherwise specified. **c-e.** Annular dark field scanning transmission electron microscopy (ADF-STEM) images and energy dispersive X-ray spectrometry (EDX) mapping of SnS_2, $SnSe_2$, and Se-doped SnS_2 (denoted as SnS_xSe_y), respectively, to show reagent-dependent tunability and doping (substitution) capability. **f-h.** ADF-STEM images and EDX mapping of semiconducting materials $MoSe_2$ (n-type), WSe_2 (p-type), and In_2Se_3 (ferroelectric), respectively.
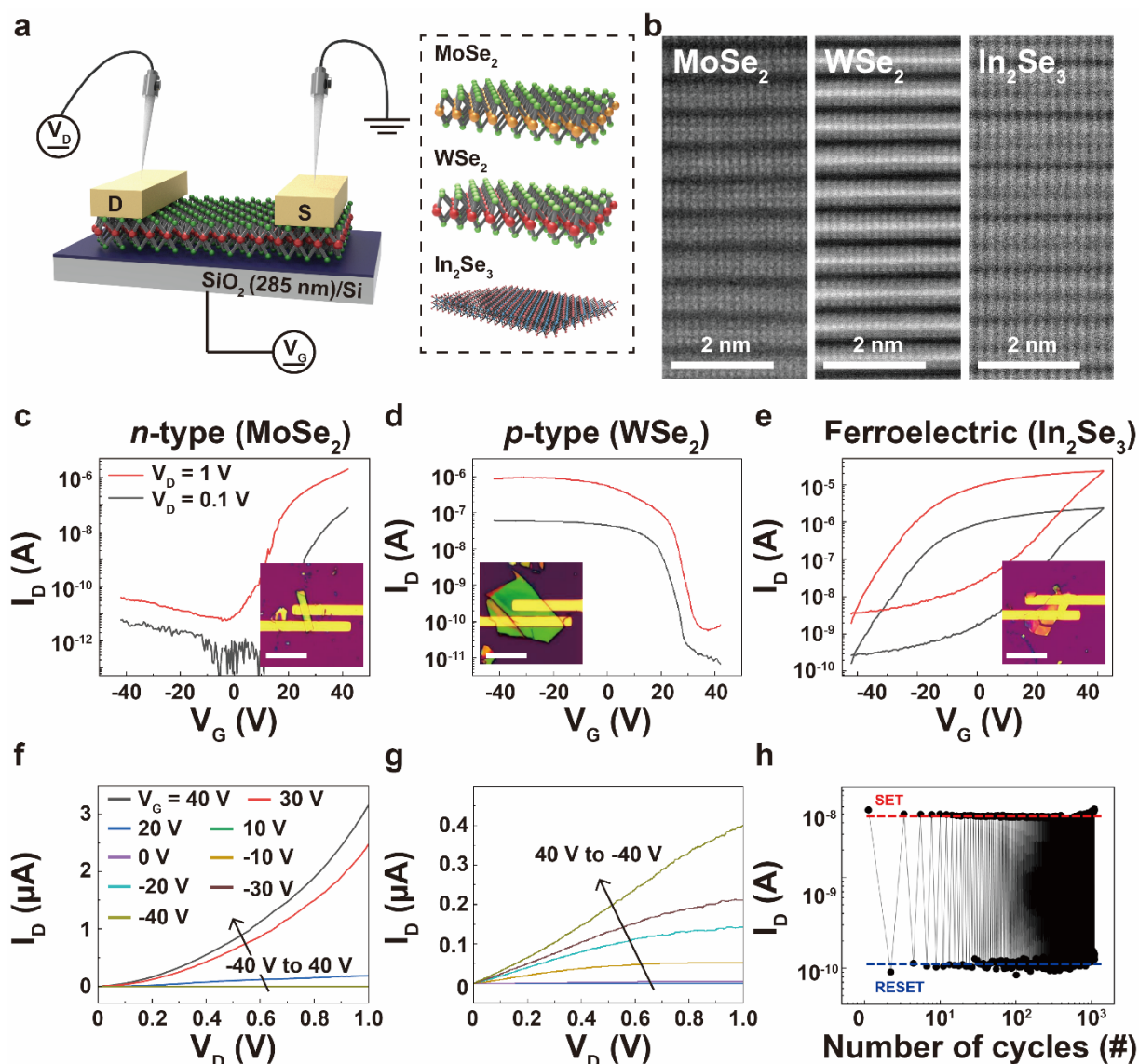
Fig. 4. Electrical properties characterization of FWF products. a. A device schematic showing experimental field-effect transistors (FET) device geometry. Schematics of crystal structure of the $MoSe_2$, WSe_2, and α-In_2Se_3 are shown in a dashed box. **b.** The cross-sectional annular dark field scanning transmission electron microscopy (ADF-STEM) images of $MoSe_2$, WSe_2, and In_2Se_3 in their respective FET devices. **c-e.** The representative transfer curves (gate-voltage (V_G)-drain current (I_D) characteristics under constant drain voltage (V_D)) for n-type $MoSe_2$, p-type WSe_2, and ferroelectric In_2Se_3 under different V_D ($V_D = 0.1$ V (black) and 1 V (red)), respectively. The figure inset shows the optical images of FET devices. The scale bar is 10 μm. **f-g.** The representative output curves (V_D-I_D characteristics under constant V_G) for n-type $MoSe_2$ and p-type WSe_2 FET devices from $V_G = -40$ V to $V_G = 40$ V, respectively. **h.** Endurance characteristics of ferroelectric In_2Se_3 FET device for 1,000 cycles. The pulse schematics are shown on the top of the figure. The operation voltages are $V_G = -40$ V (for SET) and $V_G = 40$ V (for RESET), and read voltage is $V_D = 1$ V.
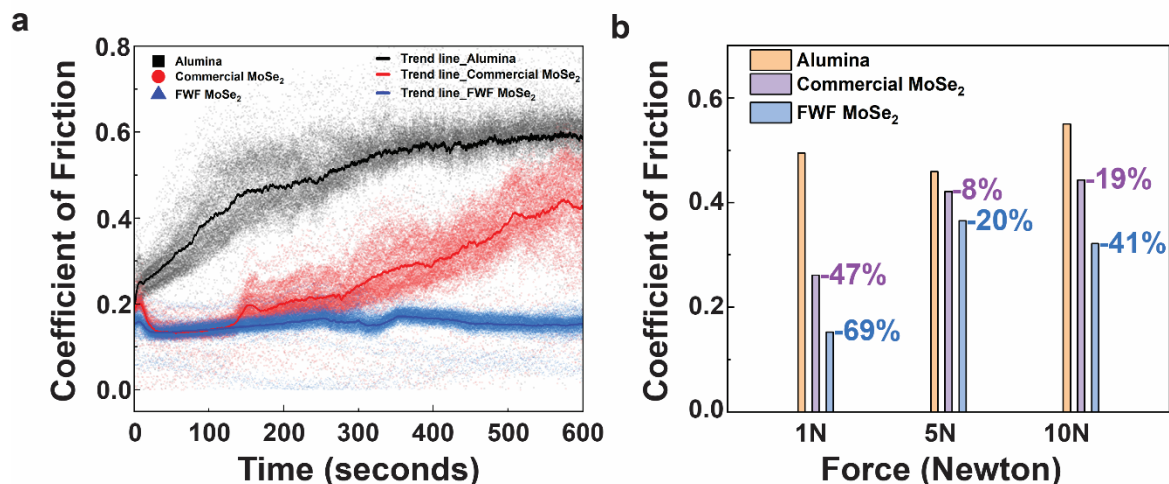
18

Fig. 5. Comparative analysis of tribological performance. a. Time-dependent coefficient of friction (COF) change for 120,000 measurements of reference alumina (denoted as blurred black squares), commercial $MoSe_2$ (denoted as blurred red circles), and FWF $MoSe_2$ (denoted as blurred blue triangles). Moving-average trend lines for the reference alumina (denoted in black line), commercial $MoSe_2$ (denoted in red line), and FWF $MoSe_2$ (denoted in blue line) under 1 N are shown concurrently. **b.** Force-dependent COF change for reference alumina, commercial $MoSe_2$, and FWF $MoSe_2$ with percentage difference in COF with respect to the reference alumina.